





# Cavity resonator-integrated guided-mode resonance filters with on-chip electro- and thermo-optic tuning

ANTOINE MONMAYRANT,<sup>1</sup> STEPHANE CALVEZ,<sup>1,\*</sup>   
PIERRE-FRANÇOIS CALMON,<sup>1</sup> PASCAL DUBREUIL,<sup>1</sup> SAMUEL  
CHARLOT,<sup>1</sup> ANNE-LAURE FEHREMBACH,<sup>2</sup> EVGUENY POPOV,<sup>2,3</sup> AND  
OLIVIER GAUTHIER-LAFAYE<sup>1</sup> 

<sup>1</sup>LAAS-CNRS, Université de Toulouse, CNRS, 7 avenue du colonel Roche, F-31400 Toulouse, France

<sup>2</sup>Aix Marseille Univ, CNRS, Centrale Marseille, Institut Fresnel, F-13013 Marseille, France

<sup>3</sup>Institut Universitaire de France, Paris, France

\*scalvez@cnsr.fr

**Abstract:** Cavity resonator grating filters (CRIGFs) integrated on lithium niobate on insulator (LNOI) with electrical tuning elements are reported. The resonance wavelength of the filters is in the 780 nm range. Integrated thermo-optical tuning range of 2.5 nm is measured using integrated resistors, whilst a 0.7 nm electro-optical tuning range using capacitive metallic pads is achieved with  $\pm 400$ V drive voltage.

© 2022 Optica Publishing Group under the terms of the [Optica Open Access Publishing Agreement](#)

## 1. Introduction

Cavity Resonator-Integrated Guided-mode Resonance Filters (CRIGFs) are planar waveguide Fabry-Perot micro-cavities with surface-normal input/output coupling provided by a finite-size intra-cavity Guided-Mode Resonance grating Filter (GMRF) [1–4]. They are used for free-space beams, acting as fixed, narrow-line, spectral filters working under focused incidence. In light of this geometry, their linear and nonlinear responses are governed by the excitation of and emission from the afferent localized Fabry-Perot modes [3,5] and typically result in a fixed-wavelength(s) passband reflection (and notch filter transmission) with Q-factors exceeding a few thousands. The latter properties are complemented by an inherently large angular tolerance [2] to form an attractive combination that can, in turn, be usefully exploited to spectrally stabilize laser diodes setup in extended-cavity configurations [6–8]. However, in contrast to other grating techniques (diffractive, volume Bragg or GMRF), CRIGFs are spectrally-insensitive to angular tuning. Wavelength-tunable devices therefore require specific implementations that either make use of a change in the micro-cavity geometric parameters or of a modification in its waveguide effective refractive index. Practical demonstrations of such tunable devices have respectively taken the form of CRIGFs with spatially-graded grating structures [9] or substrate-heated thermally-tuned CRIGFs [10].

In this paper, we report the experimental demonstration of wavelength-tunable Cavity Resonator-Integrated Guided-mode Resonance Filters which exploit the thermo-optic or the electro-optic effects induced respectively by biasing integrated resistive or capacitive electrodes. Key to this on-chip wavelength control is the fabrication of the devices on thin-film lithium niobate on insulator (LNOI) platform which offers advantageous high thermo-optic and electro-optic coefficients. Compared to [10], the reported devices pave the way towards active CRIGFs with reduced energetic driving consumption and/or faster tuning capabilities. This work, although being of some limited extent when compared to guided-optical devices [11,12], is nonetheless important because the studied devices address a completely different field of photonics. CRIGFs, like GMRFs act as narrow-band spectral filters for free-space beams. GMRFs have been harnessed

for bio-sensors [13], integrated colors filters [14], miniature spectrometers [15], laser cavity stabilization [16]. Unlike GMRFs that requires large collimated beams, CRIGFs works under tightly focused incidence offering new integration opportunities and optical geometries such as agile frequency stabilization element of cavity diode lasers [6,8] and EO TO spectral tuning of nonlinear-optical effects such as for SHG [5].

## 2. Sample design and fabrication

The CRIGFs studied here were designed for operation at a wavelength of 780 nm using the procedure described in [10] which involves thin-film scattering-matrix and waveguide effective index calculations, rigorous coupled-wave analysis [17] and coupled-mode theory [3]. More specifically, the LNOI planar waveguide consists of a 297-nm-thick X-cut LiNbO<sub>3</sub> core surrounded by a 2  $\mu\text{m}$  SiO<sub>2</sub> under-cladding layer and an upper-cladding made of a fully-etched 95 nm Si<sub>3</sub>N<sub>4</sub> grating encapsulated with 526 nm of silica. This waveguide lies on an X-cut lithium niobate substrate whose back surface was also anti-reflection coated with a single 133-nm-thick SiO<sub>2</sub> layer. The effective index of the planar waveguide with unetched (respectively etched) Si<sub>3</sub>N<sub>4</sub> layer is 2.04 (respectively 2.0). The vertical stack of the CRIGF is depicted on Fig. 1. The CRIGF central grating coupler (GC) period is  $\Lambda_{GC} = 390$  nm, with a total length of 21 periods. The lateral DBRs are 400-period long (with a period of  $\Lambda_{DBR} = \Lambda_{GC}/2 = 195$  nm and a groove width to period ratio of 50%). The length of the phase shift section (as shown on Fig. 1) is  $L_{PS} = 1.125 \Lambda_{GC}$ . The lateral extension (along the z-axis) of the CRIGFs is 15  $\mu\text{m}$ . To achieve integrated electrical tuning of the reflected spectrum, the CRIGFs were surrounded either by integrated heaters made of titanium, or by capacitive electrodes (see Fig. 1 and 2). The Ti heaters are 50- $\mu\text{m}$  wide (along the z-axis) by 200- $\mu\text{m}$  long (slightly longer than the CRIGF, which is  $\sim 170$   $\mu\text{m}$  long). For electro-optic-tuning, the capacitive Ti/Au/Al electrodes are 10  $\mu\text{m}$  wide, with a 35  $\mu\text{m}$  spacing between them (along z), and expand all along the CRIGF rows, as depicted on Fig. 2. Both kind of electrodes are deposited on top of the Si<sub>3</sub>N<sub>4</sub> grating layer (see Fig. 1).

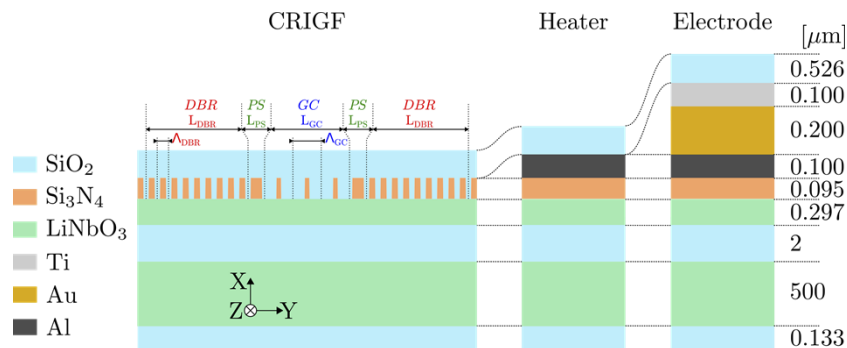


**Fig. 1.** CRIGF geometry and layers stacks schemes and dimensions.

The fabrication sequence was the following. The LNOI wafer from NanoLN was first diced into  $8 \times 12\text{-mm}^2$  samples. Then the Si<sub>3</sub>N<sub>4</sub> layer was deposited by inductively-coupled-plasma plasma-enhanced chemical vapor deposition (ICP-PECVD). The grating patterns were subsequently written using e-beam lithography and transferred into the Si<sub>3</sub>N<sub>4</sub> layer by CHF<sub>3</sub>/O<sub>2</sub>-based dry etching using the LiNbO<sub>3</sub> material as an etch-stop surface. The addition of the sets of electrodes on the sample was performed using three lithographic steps. We chose to make this patterning sequence using physical-mask-free lithography. We used direct laser writing with a Dilase 750 whose 405-nm-wavelength laser beam is focused down to a 10- $\mu\text{m}$ -diameter, 0.04-mW spot. All the mask patterns were exposed at 0.5 mm/s with 1- $\mu\text{m}$ -step overlaps and a 100- $\mu\text{m}$ -long

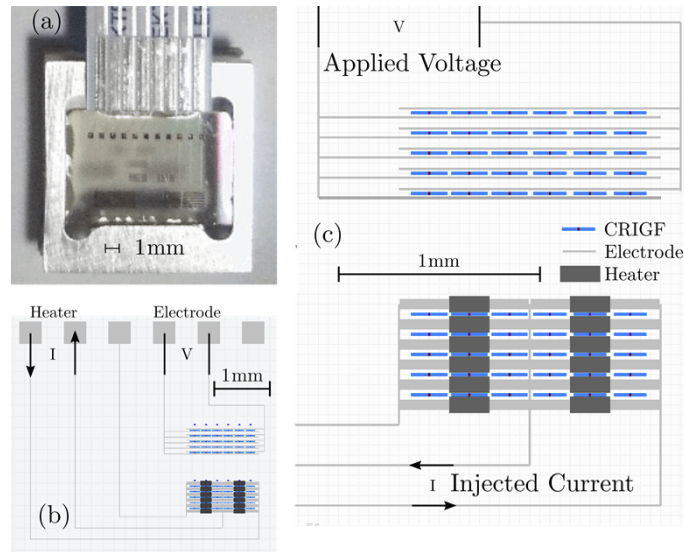


**Fig. 2.** (a) picture of the actual sample in its holder, with its connection cable. (b) General and (c) close-up view of the sample layout with the current and voltage lines highlighted. Each blue rectangle with red centers represents a CRIGF.

stabilization distance. A combination of LOR30B and SPR700 photoresists was used to create the electrode layout, with  $\sim 1\text{-}\mu\text{m}$  realignment accuracy with the previously etched grating structures. Electrode deposition was then achieved by lift-off, with an evaporated 100 nm Ti/200 nm Au/100 nm Al metal stack. The final Al layer was used to enhance adhesion of the final  $\text{SiO}_2$  layer. However, for future devices, we will rather use Cr as Al is well-known to diffuse largely into Au films, and leads to an  $\text{Al}_x\text{Au}_y$  alloy with poor electrical conductivity. The stack was left intact for the capacitive electrodes while the 60- $\mu\text{m}$ -long resistive electrodes were defined by local and selective removal of the Al and the Au layer using respectively a MF-CD-26 developer solution and a standard Au wet etchant. The deposition of the 526-nm-thick  $\text{SiO}_2$  layer and the opening of access via-holes to the contact-pads (by  $\text{CF}_4/\text{O}_2$ -based dry etching of this  $\text{SiO}_2$  layer) completed the electrode fabrication sequence (see final vertical stacks in Fig. 1). Finally, a wire bonding between the sample contact pads (450- $\mu\text{m}$ -side square) and a flat flexible connection cable was also performed to ease the electrical connection during sample testing (see Fig. 2(a)).

Preliminary electrical experiments on the sample showed an electrical resistivity of the heating metal pads of 740  $\Omega$ , largely dominated by the serial resistance of the access lines rather than by the heating elements. This stems from the poor conductivity of the alloyed Au/Al films, and means that much better electrical heating efficiencies can be achieved using better metallic alloys for the electrical lines in future devices.

### 3. Sample characterization and data analysis

The spectral reflectivity and transmission of the various CRIGFs were recorded using a 50-nm-tunable laser operating around the central wavelength of 780 nm. The fiber-coupled output beam of this source was magnified using a telescope arrangement to provide a  $\sim 8\text{-}\mu\text{m}$ -spot on the sample surface thereby allowing optimized reflection performance from the CRIGF [2].

At room temperature, the tested CRIGF exhibits a resonant reflection peak at 782.3 nm with 45% maximum and a half-width-at-half-maximum (HWHM) of 0.25 nm. When the resistive

electrodes are driven with a continuous current, the spectra are shifting toward shorter wavelength (see inset of Fig. 3). As seen on Fig. 3, the temperature elevation does not modify the width of the resonance, and a tuning range much larger than the resonance linewidth can be achieved. Here, a tuning range of 2.45 nm was achieved at maximum acceptable power of 900mW, despite the shortcomings of the heating scheme on this sample.

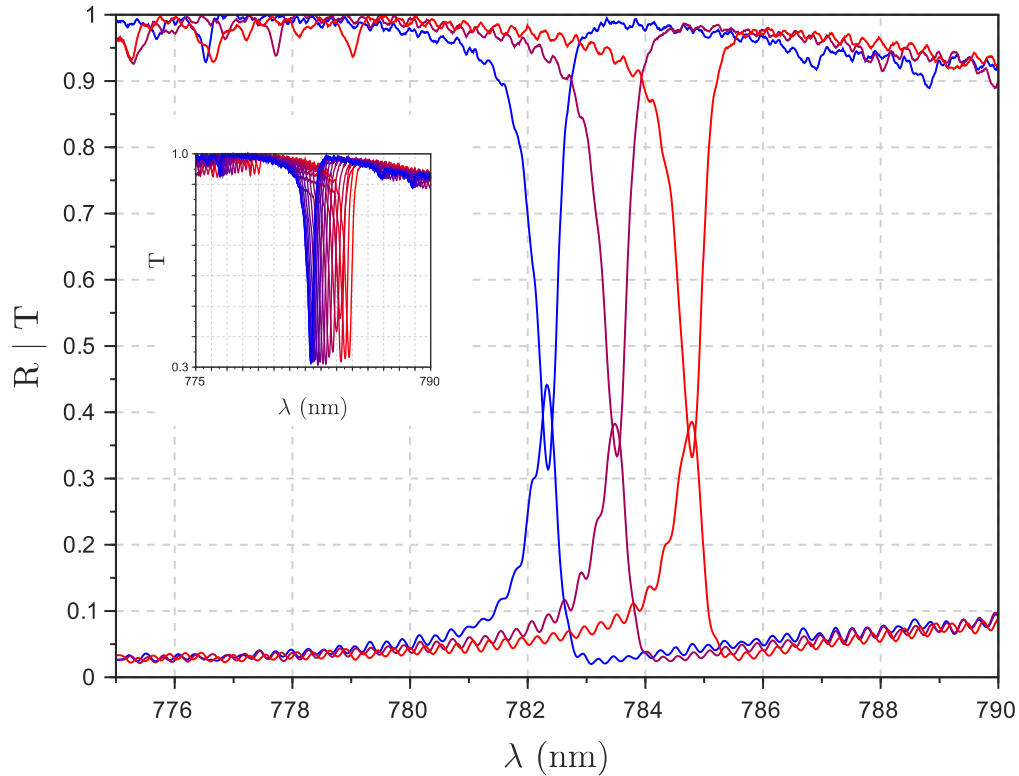


**Fig. 3.** Reflectivity and Transmission spectra for injected currents of 0 (blue), 23.1 (purple) and 29.7 mA (red). Inset: evolution of the transmission spectrum with injected currents from 0 up to 29.7 mA (from blue to red).

On Fig. 4, we plot the resonance wavelength as a function of the injected electrical power. As expected, the shift is linear with injected power with a tuning rate of 2.72 pm/mW. This tuning rate is most likely limited by the poor quality of our heaters. Indeed, instead of a localized heating of the device under study, the greater than expected resistivity of our electrical lines leads to a global heating of the sample, with strong heat dissipation in the surrounding atmosphere. Much higher efficiencies can certainly be achieved with a better heaters design. Similarly, the response time of the device was rather slow, limited by the heat diffusion and equilibrium reaching time. Smaller heating pads and heat localization structuration will certainly allow faster response in the future.

The CRIGFs with capacitive electrodes were characterized subsequently. During initial characterization, we observed a fast response of the device under study when applying a voltage across the capacitive electrodes, followed by a slow drift of the spectrum towards a stable position. So the following experimental protocol was set-up: for each applied voltage, the spectral response of the CRIGF was studied by recording a sequence of 500 15-nm-wide transmission spectra with a short sweep time of 2.7 ms each. At first, no voltage is applied ( $V = 0V$ ) then a fixed DC bias voltage is applied after the first 75 spectra. The overall dataset of 500 spectra is acquired in less

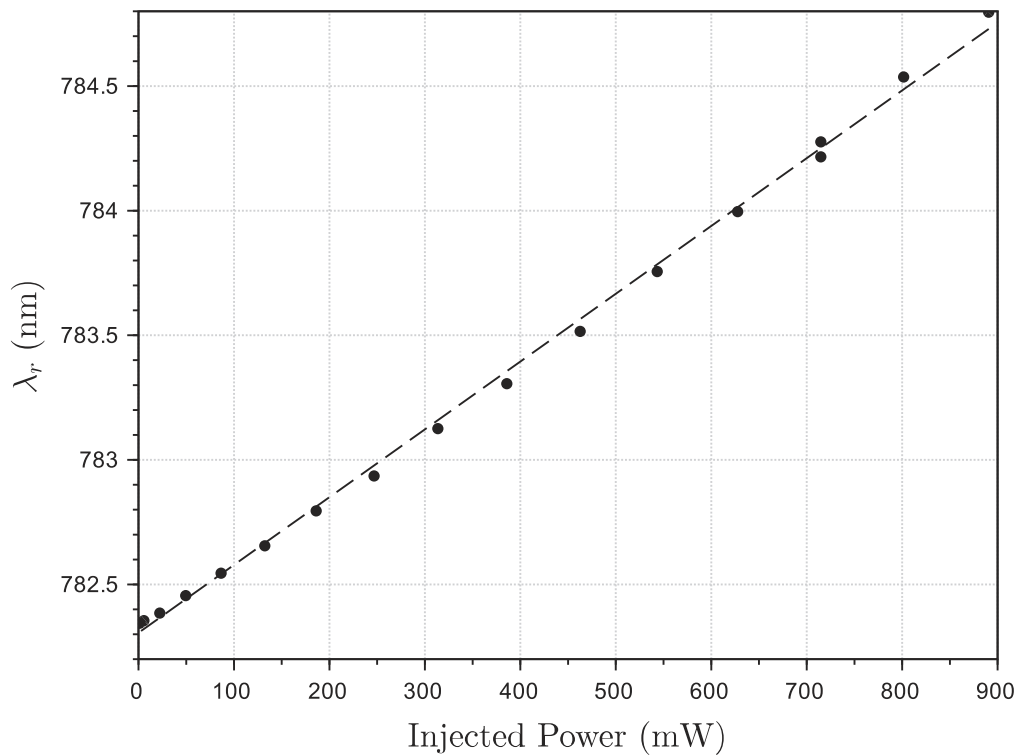


**Fig. 4.** Evolution of the resonant wavelength as a function of the injected power in the resistive heaters: experimental measurements (black dots) and the corresponding linear regression (dashed line) with a slope of 2.72 pm/mW.

than 20 s. We can then plot the maps of the transmitted (or reflected) spectra as a function of the wavelength and acquisition number (representing the elapsed time during the experiment). Typical spectral maps of the transmitted intensity versus wavelength recorded when the sample is driven with  $\pm 400$  V are shown in Fig. 5.

As seen on Fig. 5, applying the voltage tunes abruptly the resonance, with a resonance shift sign that depends on the polarity of the applied voltage. The response time is smaller than a few ms, limited by the large capacitive electrodes used in this design and the response time of our testing apparatus. At longer timescales, a slow drift towards long wavelengths is observed for both +400 V and -400 V. This slow shift is attributed to the small leakage current ( $\pm 88$   $\mu$ A for  $\pm 400$  V applied voltage, reaching the maximum output current of the K2410 voltage source used) that exists in the sample and that induces a small heating and associated small resonance shift. This shift, ( $\sim 0.2$  nm, see below) is twice larger to the one measured using resistive elements for the same dissipated power ( $\sim 0.1$  nm). This is certainly due to the greater proximity of the E-O electrodes as compared to the distributed heating elements achieved on the sample. As depicted on the inset of Fig. 6, the resonance's line-shape is not affected by the voltage, and resonance tuning of  $\sim 0.7$  nm, larger than the resonance linewidth, were experimentally achieved when changing the applied voltage from -400V to +400V.

These measurements were repeated for voltages ranging from -400V up to +400V (Fig. 5). Between each experiment, the sample was allowed to cool-down to room temperature under zero bias. Correct thermalization was checked by measuring the resonant wavelength at the beginning of the acquisition (flat green curve on Fig. 6). It was also measured just after the voltage turn-on

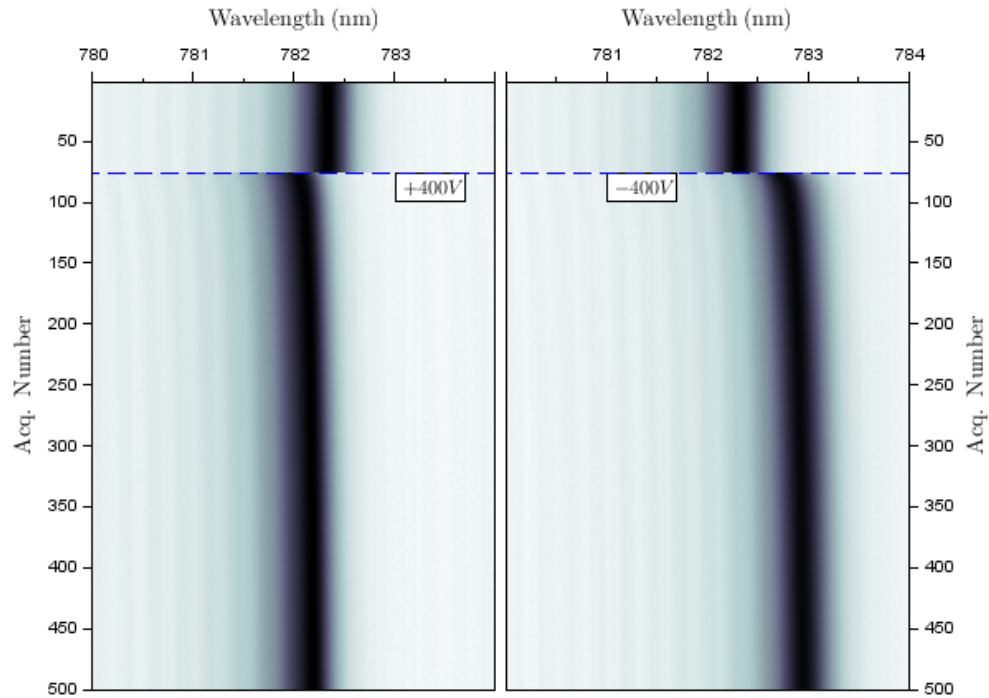


**Fig. 5.** spectral transmission maps of the evolution of the transmission spectrum upon application of a DC voltage (dashed blue line) to the capacitive electrodes: +400 V (left) and -400 V (right).

(dashed blue line on Fig. 5) to extract the quasi-athermal E-O response (blue curve on Fig. 6), and at the end of the acquisition run, when thermal equilibrium was reached (red curve on Fig. 6).

As expected, the unbiased resonant wavelength (ie wavelength before the application of the DC bias, in green in Fig. 6) is independent of the DC voltage, ensuring consistent and repeatable measurements and environmental conditions. On the same figure (red curve), the long-term stabilized resonant wavelength is shown to be asymmetric with respect to 0 V. As explained already, we believe that this asymmetry is due to a parasitic resistive heating. Looking at the response shortly after the bias application (i.e. when the influence of this long-term thermal drift can be neglected), the evolution of the resonant wavelength is more symmetric (blue curve in Fig. 6). Nevertheless, the induced wavelength shift (with respect to unbiased conditions) depends nonlinearly on the applied DC voltage, a phenomenon also observed in electro-optically controlled microring LNOI resonators [12]. This deviation from linearity suggests that there is more than the electro-optic effect at play in this dependence. In [12], it was suggested that the tuning asymmetry could be related to a slow charging process that takes place at the interface between the LN film and the surrounding dielectric layers (Maxwell–Wagner effect [13]), and dynamically modify the field penetration into the LN layer. In good agreement with this hypothesis, one can indeed see on Fig. 6 that the blue curve is not exactly symmetric around 0 V, and that its center of symmetry is slightly displaced towards positive voltages.

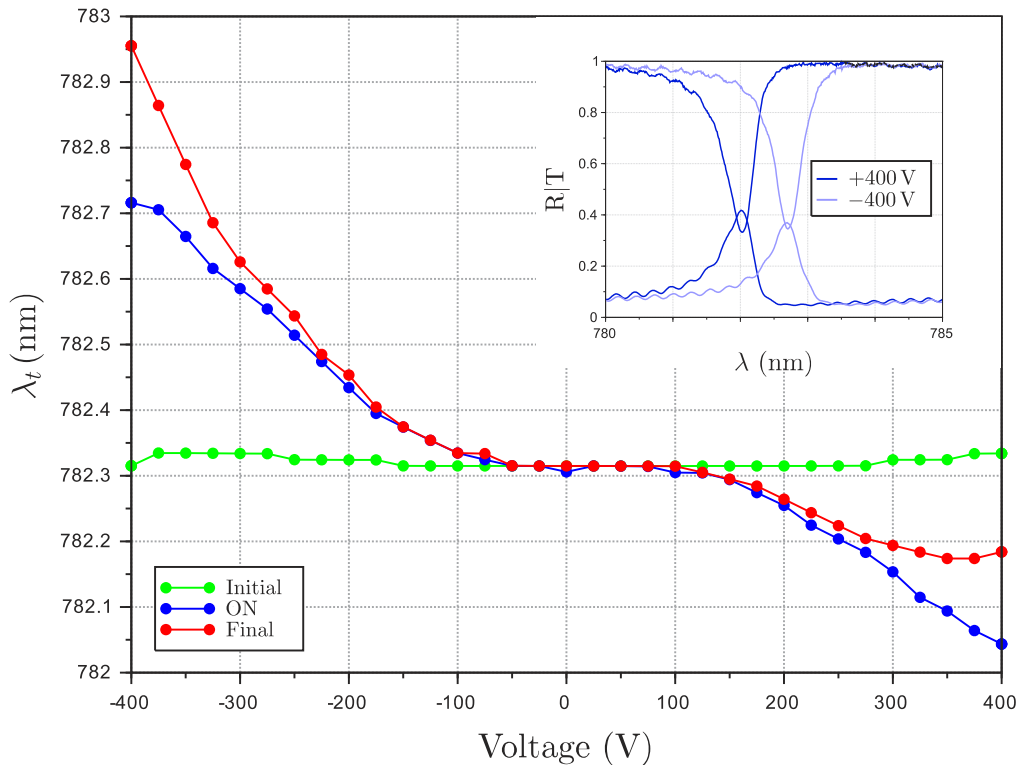


**Fig. 6.** Resonance wavelength as a function of the applied voltage. Green: wavelength before applying the voltage, blue immediately after application of the DC bias, red: at the end of the acquisition cycle. Inset: reflection and transmission spectra for an applied voltage of  $-400$  V (light blue) and  $+400$  V (dark blue).

#### 4. Conclusions

We demonstrated electrical integrated tuning of a CRIGF filter resonance made on a LiNbO<sub>3</sub> thin film. The achieved results show that the CRIGF geometry is fully compatible with a tuning strategy where “large” tuning of several nm is achieved using localized heating elements, with a linear tuning of 2,72 pm/mW, and precise, sub-nm tuning can be achieved using fast, electro-optic tuning, with a tuning of 700 pm over 800V. The obtained results, in good agreement with [12], also show that some charge diffusion process can exist when using LNOI structures that limits the electro-optical effect at low DC voltage bias.

**Funding.** Centre National d’Etudes Spatiales (R&T project 2019-1095); Agence de l’innovation de Défense (ASTRID RESON ANR-19-ASTR-0019).

**Acknowledgments.** This work was supported by LAAS-CNRS micro and nanotechnologies platform, member of the French RENATECH network. This work supported by French Defense Innovation Agency (AID) under grant ASTRID RESON ANR-19-ASTR-0019 and by CNES R&T project 2019-1095.

**Disclosures.** Authors declare no conflict of interest.

**Data availability.** Data underlying the results presented in this paper are not publicly available at this time but may be obtained from the authors upon reasonable request.

## References

1. K. Kintaka, T. Majima, J. Inoue, K. Hatanaka, J. Nishii, and S. Ura, "Cavity-resonator-integrated guided-mode resonance filter for aperture miniaturization," *Opt. Express* **20**(2), 1444–1449 (2012).
2. X. Buet, E. Daran, D. Belharet, F. Lozes-Dupuy, A. Monmayrant, and O. Gauthier-Lafaye, "High angular tolerance and reflectivity with narrow bandwidth cavity-resonator-integrated guided-mode resonance filter," *Opt. Express* **20**(8), 9322–9327 (2012).
3. R. Laberdesque, O. Gauthier-Lafaye, H. Camon, A. Monmayrant, M. Petit, O. Demichel, and B. Cluzel, "High-order modes in cavity-resonator-integrated guided-mode resonance filters (CRIGFs)," *J. Opt. Soc. Am. A* **32**(11), 1973 (2015).
4. N. Rassem, A.-L. Fehrembach, and E. Popov, "Waveguide mode in the box with an extraordinary flat dispersion curve," *J. Opt. Soc. Am. A* **32**(3), 420 (2015).
5. F. Renaud, A. Monmayrant, S. Calvez, O. Gauthier-Lafaye, A.-L. Fehrembach, and E. Popov, "Second-harmonic-generation enhancement in cavity resonator integrated grating filters," *Opt. Lett.* **44**(21), 5198–5201 (2019).
6. X. Buet, A. Guelmami, A. Monmayrant, S. Calvez, C. Tourte, F. Lozes-Dupuy, and O. Gauthier-Lafaye, "Wavelength-stabilised external-cavity laser diode using cavity resonator integrated guided mode filter," *Electron. Lett.* **48**(25), 1619–1621 (2012).
7. S. Augé, S. Gluchko, A. L. Fehrembach, E. Popov, T. Antoni, S. Pelloquin, A. Arnoult, G. Maisons, A. Monmayrant, and O. Gauthier-Lafaye, "Extended cavity quantum cascade laser with cavity resonator integrated grating filter," *Opt. Express* **28**(4), 4801 (2020).
8. A. Monmayrant, L. Ferrières, V. Lecocq, E. Feuillet, S. Denet, O. Gauthier-Lafaye, and B. Faure, "Cavity Resonator Integrated Filter (CRIGF) Based External Cavity Laser in a Butterfly Package," in *2019 21st International Conference on Transparent Optical Networks (ICTON)* (2019), pp. 1–3.
9. S. Augé, A. Monmayrant, S. Pelloquin, J. B. Doucet, and O. Gauthier-Lafaye, "Tunable graded cavity resonator integrated grating filters," *Opt. Express* **25**(11), 12415 (2017).
10. S. Calvez, A. Monmayrant, and O. Gauthier-Lafaye, "Thermally-tunable cavity resonator-integrated guided-mode resonance filters," *OSA Continuum* **2**(11), 3204 (2019).
11. M. R. Escalé, D. Pohl, A. Sergeev, and R. Grange, "Extreme electro-optic tuning of Bragg mirrors integrated in lithium niobate nanowaveguides," *Opt. Lett.* **43**(7), 1515 (2018).
12. M. Bahadori, Y. Yang, A. E. Hassani, L. L. Goddard, and S. Gong, "Ultra-efficient and fully isotropic monolithic microring modulators in a thin-film lithium niobate photonics platform," *Opt. Express* **28**(20), 29644 (2020).
13. R. Magnusson, "The Complete Biosensor," *J. Biosens. Bioelectron* **04**(02), 1 (2013).
14. M. J. Uddin and R. Magnusson, "Highly efficient color filter array using resonant Si<sub>3</sub>N<sub>4</sub> gratings," *Opt. Express* **21**(10), 12495 (2013).
15. H.-A. Lin, H.-Y. Hsu, C.-W. Chang, and C.-S. Huang, "Compact spectrometer system based on a gradient grating period guided-mode resonance filter," *Opt. Express* **24**(10), 10972 (2016).
16. L. Guillemot, T. Oksenhendler, S. Pelloquin, O. Gauthier-Lafaye, A. Monmayrant, and T. Chanelière, "Guided-mode resonance filter extended-cavity diode laser," *Laser Phys.* **30**(3), 035802 (2020).
17. P. C. Chaumet, G. Demésy, O. Gauthier-Lafaye, A. Sentenac, E. Popov, and A.-L. Fehrembach, "Electromagnetic modeling of large subwavelength-patterned highly resonant structures," *Opt. Lett.* **41**(10), 2358 (2016).